Radio Science, Volume ???, Number , Pages 1–15,

Elevation Angle Determination for SuperDARN HF Radar Layouts

S. G. Shepherd

Thayer School of Engineering, Dartmouth College, Hanover, New Hampshire, USA

Key Points.

- An algorithm for accurately determining the elevation angle of HF signals is presented for general SuperDARN radar layouts.
- Small differences with the standard algorithm are shown to exist.
- More flexibility in radar layout is provided by using the more general algorithm.

The international scientific radars known as the Super Dual Auroral Radar Network (SuperDARN) are designed to primarily measure plasma convection at ionospheric altitudes over a large region of the northern and southern hemispheres. SuperDARN radars are equipped with a secondary interferometry array that is used to measure the elevation angle (α) of signals. These values of α have been used in relatively few studies, however, they are important for estimating ionospheric quantities and for accurate geolocation of the ionospheric source region of backscattered signals. The majority of SuperDARN radars are constructed with interferometers that are separated from their main array in one or two dimensions and a relatively straightforward algorithm gives reasonably accurate results. A solution to the more general case, where offsets in all three dimensions are present, is desirable for future designs and necessary for at least one operational radar. Details of such an algorithm are described here and applied to phase measurements from several radars. For radars with interferometers offset only along the radar boresight and vertical directions, small differences of up to $\sim$1.5° in α are observed and negative values of α, which are deemed unphysical, are no longer produced. For the radar interferometer that is offset in all three dimensions the resulting values of α are consistent with expected behavior. The algorithm presented here provides a technique for accurately determining α from SuperDARN radars with offsets in all three dimensions and significantly reduces constraints placed on the positioning of interferometers for future SuperDARN radars.

1. Introduction

The international network of low-power, high-frequency (HF) radars known as the Super Dual Auroral Radar Network (SuperDARN) makes measurements of the drifting plasma at ionospheric altitudes in Earth's polar regions for scientific purposes. Numerous studies of atmospheric, ionospheric and magnetospheric phenomenon have been made possible with data from SuperDARN over the past several decades [*Greenwald et al.*, 1995; *Chisham et al.*, 2007]. The network has been expanding in both longitudinal and latitudinal extents since the first radar was installed in Goose Bay, Labrador (gbr), and now comprises 35 operational radars in the northern and southern hemispheres, with several additional radars in the planning and construction stages (see Table 1 for 3-character radar IDs and relevant interferometer parameters. A more comprehensive table and figures showing radar locations can be found at `superdarn.thayer.dartmouth.edu` and as supplementary material.)

While individual radars can differ in many respects, the radars all conscribe to several fundamental design principles including the use of a linear, phased array of 16 antennas that transmit and receive horizontally polarized HF signals in the 8–20 MHz range. Two antenna styles are predomi-

0048-6604/17/$11.00

nantly used for SuperDARN radars, a log-periodic dipole (LPD) and a twin-terminated, folded dipole (TTFD). The performance characteristics vary somewhat, but they both operate in a similar fashion [*Custovic et al.*, 2013].

SuperDARN radars operate at HF frequencies in order to obtain sufficient refraction and achieve perpendicularity to the magnetic field-align density irregularities from which signals backscatter at ionospheric altitudes [c.f., *Baker et al.*, 1983; *Greenwald et al.*, 1985] The radars operate at a specified frequency within the 8–20 MHz range in order to maximize backscatter returns depending on the variable ionospheric density or for a particular scientific objective. The standard radar operating mode is to scan sequentially through 16 to 24 predetermined beam directions in a period of 1–2 minutes. More complex modes, such as the inclusion of a camping beam, which samples one beam direction (the camping beam) on alternate soundings, are possible depending on scientific objectives of individual radars or the network as a whole. More details of the operational capabilities of SuperDARN radars can be found in the reviews by *Greenwald et al.* [1995] and *Chisham et al.* [2007].

The linear array and electronic phasing allow for the formation and steering of a beam that is $\sim 3^\circ$ wide in the azimuthal direction. In the vertical direction the beam is much broader and signals can be received from a wide range of elevation angles (α). Knowledge of α from backscattered signals can be important for determining the mode of propagation (multi-hop returns, in which the radio wave travels between the Earth and ionosphere multiple times before returning to the radar, are common at HF), for accurately locating measurements (particularly those that are multi-hop) [*Yeoman et al.*, 2001, 2008] and for estimating ionospheric parameters such as the electron density [*André et al.*, 1998; *Ponomarenko et al.*, 2011], the maximum usable frequency (MUF) [*Hughes et al.*, 2002; *Bland et al.*, 2014] and the index of refraction in the ionosphere [*Gillies et al.*, 2009].

In order to determine α of backscattered signals SuperDARN radars employ a secondary linear array (interferometer) of similar design to the main array that is spatially separated from the main array. By measuring the phase difference between backscattered signals that are observed by the two arrays, α can be determined using known information about the radar configuration. With the exception of the original SuperDARN radar (gbr) which used a full 16-antenna interferometer array for a brief period, interferometer arrays use four receive-only antennas resulting in a wider beam and lower gain. The smaller interferometer array has been shown to be adequate for determining α [*Greenwald et al.*, 1995; *Custovic et al.*, 2013] and has the distinct advantage of overall lower construction cost and more flexibility in antenna array layout, particularly with dual radar sites where two SuperDARN radars (four arrays) are located at a single location and share a common equipment shelter (e.g., adw-ade, cvw-cve, fhw-fhe).

Most SuperDARN radars are configured with the interferometer array offset from the main array only along the direction of the radar boresight. In these cases the algorithm for determining α is quite straightforward [*Milan et al.*, 1997]. The local terrain or property boundaries can, however, dictate that the interferometer array be offset in one or more additional directions and the resulting algorithm for determining α becomes more complicated. An algorithm that can be applied to the general case where the offset is in all three dimensions has never been employed on SuperDARN radars.

An algorithm for determining α for general SuperDARN radars layouts is presented here and applied to several configurations. Results are compared to those obtained using the present algorithm. For the majority of radars the differences are small, however, for layouts that have larger offsets in one or more additional directions the differences can be significant. The general algorithm has the distinct advantage of removing any restriction on interferometer placement; an improvement that potentially makes additional sites available for locating the large arrays and reduces site construction costs by eliminating the need to raise or lower the height of the interferometer array in order to level it with the main array.

2. SuperDARN Radar Array Layout

The coordinate system shown in Figure 1 is used to describe the algorithm for a general interferometer configuration. The origin of the coordinate system is located at the center of the main array with the radar boresight (direction of maximum gain) defining the $\hat{y}$-direction, $\hat{z}$ is in the vertical direction and $\hat{x}$ completes the right-handed orthogonal set.

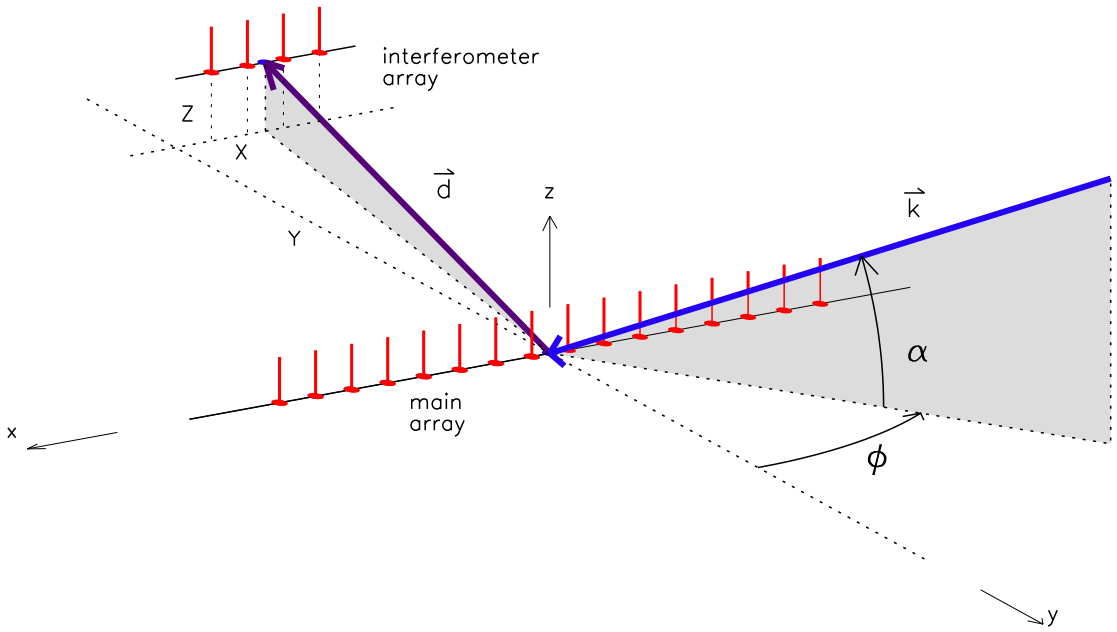

Figure 1. Example of main and interferometer array positions for a representative SuperDARN layout. Positions of antennas are indicated by red dots and vertical line-segments. The origin is located at the center of the main array and the position of the interferometer array $\vec{d} = X\hat{x} + Y\hat{y} + Z\hat{z}$, shown by the purple vector. The incident plane wave vector $\vec{k} = -k(\hat{x}\cos\alpha\sin\phi + \hat{y}\cos\alpha\cos\phi + \hat{z}\sin\alpha)$ is shown by the blue vector.

In this coordinate system the center of the interferometer array is located at the position given by the vector $\vec{d} = X\hat{x} + Y\hat{y} + Z\hat{z}$. In the example shown in Figure 1 the interferometer array is situated behind and above the main array so that $Y < 0$ and $Z > 0$, while $X < 0$. For the purposes of the derivation given here it is assumed that all antennas in a given array are at the same vertical height and that the two arrays are oriented parallel to each other, i.e., they share a common boresight direction.

There are two aspects of SuperDARN radar design that introduce a phase difference between the signals received by the two arrays: a geometric factor due to the spatial separation of the arrays and a factor due to the difference in the electrical path lengths that signals travel between the respective antennas and the digitizer. Knowledge of both factors are required for accurate determination of α and are specified for each radar. The geometric factor is specified by the offsets (X, Y, Z) and given in meters while the electrical factor is specified as a time delay (t_{diff}) and given in microseconds. A positive value of t_{diff} indicates that the electrical path is longer for the interferometer array than it is for the main array. Table 1 contains a list of the geometric offsets (X, Y, Z) and t_{diff} values for the 35 operational (as of April 2017) SuperDARN radars; identified by their unique three-letter code in the first column.

Table 1. Array separations and time delay differences for the current operational SuperDARN radars, circa 2017, indicated by 3-character IDs. Radars with nonzero array offset components for Y only, Y and Z, Y and X, all three, are shown in black, blue, green and red, respectively.

Radar ID	X (m)	Y (m)	Z (m)	t_{diff} (μs)
ade	0.0	-69.85	+0.5	-0.435
adw	0.0	-69.85	0.0	-0.421
bks	0.0	-58.9	-2.7	-0.338
bpk	0.0	-80.0	0.0	0.000
cly	0.0	+100.0	0.0	0.000
cve	0.0	-80.0	0.0	-0.398
cvw	0.0	-80.0	0.0	-0.351
dce	0.0	-90.0	0.0	-0.151
fhe	0.0	-80.0	0.0	
fhw	0.0	-80.0	0.0	
gbr	+1.5	+100.0	0.0	+0.478
hal				
han	0.0	+185.0	-2.2	+0.181
hkw	0.0	-100.0	+2.55	
hok	0.0	-100.0	+2.9	
inv	+1.5	+100.0	0.0	0.000
kap	0.0	+100.0	-2.0	+0.043
ker	0.0	-89.6	0.0	0.000
kod	0.0	-100.0	0.0	0.000
ksr	0.0	+100.0	0.0	0.000
lyr	0.0	-100.1	+8.1	
mcm	0.0	+70.1	-4.1	0.000
pgr	0.0	-100.0	0.0	0.000
pyk	0.0	+100.0	0.0	-0.083
rkn	0.0	-100.0	0.0	0.000
san	0.0	+100.0	0.0	0.000
sas	0.0	-100.0	0.0	0.000
sps	0.0	+97.5	0.0	+0.192
sto	0.0	+100.0	0.0	0.000
sye	0.0	+91.9	0.0	0.000
sys	0.0	+91.9	0.0	0.000
tig	0.0	-100.0	0.0	0.000
unw	0.0	-100.0	0.0	0.000
wal	0.0	+100.0	0.0	
zho	-27.6	+100.1	-5.3	-0.180

The main cause for a nonzero t_{diff} is the difference in cable lengths that transmit signals from the antennas to the equipment shelter. For instance, at the radars located near Christmas Valley, Oregon (cvw and cve) the cables to the antennas in the main arrays are ∼650 feet in length whereas the corresponding cables to the antennas in the interferometer array are only ∼350 feet. The difference of ∼400 feet results in a value of t_{diff} that is approximately -0.4 microseconds. Note that there are additional differences in path lengths in the electronics of these two radars that also contribute to t_{diff}.

The value of t_{diff} is typically measured at the time a radar is constructed or when major changes are made that require the value to be re-measured, however this measurement can, in some cases, be difficult to perform and it can depend on other parameters such as temperature, age, frequency, beam direction and other less-measurable parameters. The subject of the reliability of t_{diff} is left for another study, but it is acknowledged that uncertainties in t_{diff} can lead to inaccurate estimates of α. For the purposes of the algorithm derived here it is assumed that t_{diff} is a constant that can be determined for a given radar.

The position of the interferometer array is the primary design factor that affects the measurement of α. Because SuperDARN radar beam directions are limited to $\sim \pm 30°$ of azimuth from the radar boresight direction, the main factor in introducing a phase shift in the signals received by the two arrays is the $\hat{y}$-direction and for all SuperDARN radars $Y \gg X, Z$.

As shown in Table 1 the majority of SuperDARN radars have only nonzero values for the Y offset, i.e., $X = Z = 0$. Interferometers can be located in front of ($Y > 0$) or behind ($Y < 0$) the main array. The separation distance (Y) varies between ∼60–185 m, but is typically around 100 m. Note that this typical separation corresponds to just over three full wavelengths for a radar operating at 10 MHz, which leads to an ambiguity in α (discussed in more detail in section 3.) To eliminate any ambiguity in α the separation distance (d) would ideally be exactly one wavelength (∼30 m at 10 MHz), or half of one wavelength when considering both front and back lobes, i.e., signals arriving from behind the radar. While such a separation is possible for a single frequency, it is not possible for the >10 MHz frequency range over which SuperDARN radars can operate, but does suggests that a reduction in the typical separation would be more desirable. The fact that shadowing of the rear array or coupling between the arrays can occur if the separation is too small, however, suggests that the separation should be larger [*Custovic et al.*, 2013]. One SuperDARN radar in Buckland Park, Australia (bpk) employs a unique design with two interferometer arrays, one in front and one behind the main array for the purpose of eliminating the ambiguity associated with determining elevation angles [*McDonald et al.*, 2013; *Custovic et al.*, 2013]. For all other SuperDARN radars a compromise is made between these two competing factors and as a result some ambiguity remains in determining α.

The main factors that dictate the need for interferometers to be offset in the $\hat{x}$ or $\hat{z}$ directions are terrain and property boundaries. The area required for a single SuperDARN radar is on the order of 150 m × 250 m. Finding an area of this size that is flat and oriented in the desired direction can be chal-

lenging and a compromise must often be made in which the interferometer array is located at a different height (nonzero Z) or shifted along the direction of the array (nonzero X). The alternative is costly site excavation or the addition of material in order to lower or raise the height of antennas in one array. Table 1 shows that several radars have nonzero Z offsets (shown in blue) that range up to 8 m in magnitude, fewer radars with small, nonzero X offsets (shown in green) of ∼1 meter and one radar (zho in red) that has relatively large offsets for both X and Z.

It should be noted that the original interferometer at Goose Bay, Labrador (gbr) had a relatively large offset of $X = 15.5$ m. The interferometer was subsequently reduced from 16 to 4 antennas and moved to reduce the offset to $X = 1.5$ m, in part because of unsatisfactory results in measuring α. In addition, the interferometers at the Syowa Station radars in Antarctica (sye and sys) were moved after initial construction to eliminate the offsets in both X and Z. The need for such costly actions will no longer be necessary.

3. Angle-of-Arrival Determination

As shown in Figure 1, the separation between the main and interferometer arrays is given by the vector

$$\vec{d} = X\hat{x} + Y\hat{y} + Z\hat{z} \tag{1}$$

The wave vector of an incident plane wave propagating through free space in the direction given by the two angles α and ϕ is

$$-\vec{k} = \frac{2\pi f_{\mathsf{TX}}}{c}\left[\cos\alpha\sin\phi\hat{x} + \cos\alpha\cos\phi\hat{y} + \sin\alpha\hat{z}\right] \tag{2}$$

The negative sign on $\vec{k}$ is necessary for the wave that is incident on the arrays, i.e., the backscattered signal. The angle α is the elevation angle from the x-y plane (i.e., what we are looking for), the angle ϕ is the angle from the boresight direction toward the $+\hat{x}$ direction, f_{TX} is the radar transmission frequency and c is the speed of light in free space.

The phase difference between plane waves arriving at the main and interferometer arrays is then given by

$$\psi_{\mathsf{GEO}} = -\vec{k}\cdot\vec{d} \tag{3}$$

which is the phase difference between two parallel planes normal to $\vec{k}$ and separated by the distance d, one containing the origin (the center of the main array) and the other containing the point (X, Y, Z); the center of the interferometer array. The subscript on ψ_{GEO} indicates that it is due to the geometric separation of the two arrays.

Note ϕ is not the beam (main lobe) direction set by the phasing electronics, i.e., at $\alpha = 0°$ which is represented here by ϕ_0. The beam direction (ϕ) of a linear array of antennas forms a cone around the array axis ($\hat{x}$) and therefore depends on α. It can be easily shown that ϕ of a beam resulting from a linear array is given by

$$\sin\phi = \frac{\sin\phi_0}{\cos\alpha} \tag{4}$$

where ϕ_0 is the azimuthal angle in the x-y plane, i.e., where $\alpha = 0°$ and set by the phasing electronics.

Equation 4 can be rewritten using trigonometric identities as

$$\cos\phi = \frac{\left(\cos^2\phi_0 - \sin^2\alpha\right)^{\frac{1}{2}}}{\cos\alpha} \tag{5}$$

and then used with equation 4 to rewrite equation 3 in terms of the known quantities as

$$\psi_{\mathsf{GEO}} = \frac{2\pi f_{\mathsf{TX}}}{c}\left[X\sin\phi_0 + Y\left(\cos^2\phi_0 - \sin^2\alpha\right)^{\frac{1}{2}} + Z\sin\alpha\right] \tag{6}$$

The additional phase introduced by a difference in the electrical path lengths that signals must make from the respective arrays to the digitizer depends on f_{TX} and is given by

$$\psi_{\mathsf{ELE}} = -2\pi f_{\mathsf{TX}} t_{\mathsf{diff}} \tag{7}$$

and the total phase difference is the sum of equations 6 and 7

$$\psi_{\mathsf{TOT}} = \psi_{\mathsf{GEO}} + \psi_{\mathsf{ELE}} \tag{8}$$

which is in terms of the known radar parameters $(X, Y, Z, t_{\mathsf{diff}})$ listed in Table 1, f_{TX}, ϕ_0 and $\sin\alpha$. The latter is determined by equating equation 8 to the observed phase difference (ψ_{OBS}) and solving for α.

3.1. Simple Case: $X = Z = 0$

For most operational SuperDARN radars $X = Z = 0$ and equation 8 simplifies considerably. In this case the solution for α can be written as

$$\sin\alpha = \left[\cos^2\phi_0 - \frac{(\psi_{\text{OBS}} - \psi_{\text{ELE}})^2}{k^2 Y^2}\right]^{\frac{1}{2}} \qquad (9)$$

which is equivalent to equation (4) given by *Milan et al.* [1997], who use Δ instead of α for the elevation angle and Ψ for the equivalent of $\psi_{\text{OBS}} - \psi_{\text{ELE}}$ in equation 9.

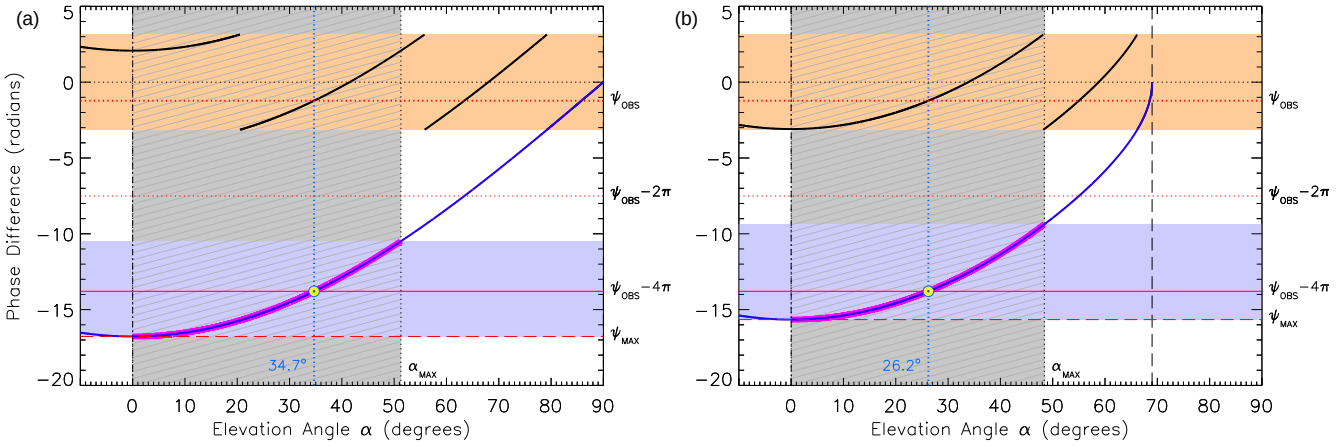

Figure 2. Total phase difference ψ_{TOT} (shown in solid blue) for a beam directed (a) along the radar boresight ($\phi_0 = 0°$) and (b) away from the radar boresight ($\phi_0 = 21°$). The gray shaded and hatched region corresponds to the range of measurable elevation angles: $\alpha = [0°, \alpha_{\text{MAX}}]$, also highlighted by the thick magenta line segment. The blue-gray shaded region represents the range of ψ_{TOT} over this measurable region: $\psi_{\text{TOT}} = [\psi_{\text{MAX}}, \psi_{\text{MAX}} - 2\pi]$. The orange shaded region represents the range of $\psi_{\text{OBS}} = [-\pi, \pi]$. The solution for α is given by the intersection of the curve for ψ_{TOT} and the value of ψ_{OBS}, shifted by the appropriate factors of 2π, and indicated by the yellow dot. Black line segments represent the relative phase of ψ_{TOT}, illustrating the ambiguity in α.

Figure 2 shows an example of the procedure used for determining α for a particular radar configuration. The configuration selected is relatively common and similar to the cvw SuperDARN radar. In this case the interferometer offsets are $(X, Y, Z) = (0.0, -80.0, 0.0)$ meters and a representative value of $f_{\text{TX}} = 10.0$ MHz is chosen. Figure 2a shows the case for a beam directed along the radar boresight ($\phi_0 = 0°$) and Figure 2b shows the case for a beam directed 21° from the boresight direction ($\phi_0 = 21°$), i.e., approximately six beams from the boresight.

The solid blue curve in Figure 2 represents ψ_{TOT}, the total phase difference observed as a function of α. The maximum phase difference occurs at $\alpha = 0°$ and is negative because the interferometer is located behind the main array ($Y < 0$), thus signals arrive first at the main array.

As stated in section 2, the array separation ($Y = -80$ m) is larger than the wavelength of the backscattered signal and an ambiguity is therefore introduced. With a single interferometer it is only possible to measure the relative phases of the signals received by the two arrays. The measured or observed phase difference (ψ_{OBS}) is therefore limited to the range $[-\pi, \pi]$ and indicated by the orange shaded regions of Figure 2. The true phase difference (ψ_{TOT}), however, extends over several 2π intervals. Black line segments within the orange shaded regions represent

the relative phases that are observed as a function of α. To be clear, the total phase difference (blue curve) is what is desired for the solution, however only the relative phase (black line segments) is observed.

In order to determine a solution for α, ψ_{OBS} must be mapped to the appropriate 2π interval. Because of the phase ambiguity a few assumptions must be made. First, it is assumed that the backscattered signal comes from in front of the radar. *Milan et al.* [1997] investigate signals that are thought to be detected in the radar back lobes. While it is possible to consider this situation in the analysis presented here, it is left out for the sake of simplicity. The other assumption made here is that α is from the lowest range observable. That is, ψ_{OBS} is mapped to the range $[\psi_{\mathsf{MAX}},\ \psi_{\mathsf{MAX}} \pm 2\pi]$, where the sign depends on the sign of Y; positive for $Y < 0$ and negative for $Y > 0$. This choice is made, in part, from the results of ray-tracing studies showing high elevation angle rays penetrating the ionosphere rather than undergoing sufficient refraction to achieve perpendicularity and backscattering at ionospheric altitudes [c.f., *Villain et al.*, 1984; *André et al.*, 1997; *de Larquier et al.*, 2013].

In Figure 2, the blue-gray shaded regions indicate the range to which ψ_{OBS} is mapped, i.e., $[\psi_{\mathsf{MAX}},\ \psi_{\mathsf{MAX}} \pm 2\pi]$. Note that this range corresponds to a limited range of α which extends from 0° to α_{MAX}; demarked by the gray shaded and hatched region. The thick magenta line segment highlights the range of α that the algorithm produces. Because of the inherent ambiguity values of $\alpha > \alpha_{\mathsf{MAX}}$ are aliased into the range of observable α.

The mapping of ψ_{OBS} to the appropriate range is achieved by adding an appropriate number (n) of 2π factors. In order to determine n, ψ_{MAX} must first be determined. Note that in the case where $Z = 0$ the value of ψ_{MAX} occurs when $\alpha = 0^\circ$. However, the maximum phase difference occurs when $\vec{k}$ and $\vec{d}$ are parallel and ψ_{MAX}, therefore, corresponds to a nonzero value of α when $Z \neq 0$. In general, the value of α where ψ_{MAX} occurs is where the gradient of ψ_{TOT} with respect to α is zero, or

$$\frac{\partial \psi_{\mathsf{TOT}}}{\partial \alpha} = \frac{2\pi}{c f_{\mathsf{TX}}} \Bigg\{ -Y \left[\frac{\cos\alpha \sin\alpha}{\left(\cos^2\phi_0 - \sin^2\alpha\right)^{1/2}} \right] + Z\cos\alpha \Bigg\} = 0 \tag{10}$$

Using trigonometric identities, equation 10 can be solved for the value of α at which ψ_{MAX} occurs, defined here as α_0, and given by

$$\sin\alpha_0 = \frac{Y}{|Y|} \frac{Z\cos\phi_0}{\left(Y^2 + Z^2\right)^{1/2}} \tag{11}$$

where the sign of α_0 depends on the signs of both Y and Z. It can be seen from equation 11 that if $Z = 0$ then $\alpha_0 = 0^\circ$.

It is worth noting that some confusion with symbol subscripts is possible. The values of ϕ_0 and α_0 are related by equation 11, but to be clear, ϕ_0 is the beam direction set by the phasing matrix, i.e., at $\alpha = 0^\circ$, whereas α_0 is the elevation angle at which ψ_{MAX} occurs, not necessarily at $\alpha = 0^\circ$. Furthermore, the MAX subscript on ψ_{MAX} and α_{MAX} are used to indicate maximum values of each quantity but they are not directly related.

The correct number of 2π factors (n) can then be determined by evaluating equation 8 for ψ_{TOT} using the value of α_0 from equation 11 and giving the value of ψ_{MAX}. The number of 2π factors is

$$n = \begin{cases} \texttt{floor}\left[\left(\psi_{\mathsf{MAX}} - \psi_{\mathsf{OBS}}\right)/(2\pi)\right] & : \quad Y > 0 \\ \texttt{ceil}\left[\left(\psi_{\mathsf{MAX}} - \psi_{\mathsf{OBS}}\right)/(2\pi)\right] & : \quad Y < 0 \end{cases} \tag{12}$$

where the `floor` and `ceil` functions are the standard functions that round toward negative and positive infinity, respectively.

The value of α is then determined from the intersection of ψ_{TOT} with ψ_{OBS} mapped by the correct number of 2π factors, i.e., by solving the equation

$$\psi_{\mathsf{TOT}} = \psi_{\mathsf{GEO}} + \psi_{\mathsf{ELE}} = \psi_{\mathsf{OBS}} + n2\pi \tag{13}$$

The solution is indicated by the yellow dot in Figure 2; the intersection of the horizontal solid red line ($\psi_{\mathsf{OBS}} + n2\pi$) and ψ_{TOT}. Note that the value of $\psi_{\mathsf{OBS}} = -0.39\pi$ is simply chosen to give a representative value of α for the example shown in Figure 2.

While a more complete discussion of aliasing associated with α is given by *McDonald et al.* [2013], the issue is illustrated in Figure 2 where the value of ψ_{OBS} intersects the relative phase curves (black line segments) at multiple locations in the upper shaded region. These intersections correspond to the same value of α, i.e., values of $\alpha > \alpha_{\mathsf{MAX}}$ are aliased to a value below α_{MAX}.

It should also be noted that the value of ψ_{MAX} decreases as ϕ_0 is moved away from the boresight direction (as seen in Figure 2.) In addition, a steeper gradient in the total phase is associated with the dependence of ϕ on α, as given by equation 4. The result is a smaller α_{MAX} for beams directed away from the radar boresight, as shown by the smaller hatched region in Figure 2b. Furthermore, the maximum observable value of α is given by $90^\circ - \phi_0$ and is indicated by the vertical dashed line in Figure 2b.

Note that for this example the value of t_{diff} is set to zero in order to clarify the procedure. A nonzero value of t_{diff} affects ψ_{ELE}, which does not depend on α and therefore acts to merely shift ψ_{TOT} up or down along the y-axis in Figure 2. In the case of cvw, $t_{\mathsf{diff}} = -0.351\mu$s and the curve for ψ_{TOT} is shifted closer to zero, which only adds confusion to the solution process. A value of $t_{\mathsf{diff}} = 0\mu$s indicates that the electrical paths are the same for each array (as is the case for many radars) but does not affect the ambiguity in determining α that is associated with the array separation.

3.2. General Case: $X, Y, Z \neq 0$

For the more complicated case where the interferometer has offsets in more than just the $\hat{y}$-direction, i.e., $X, Y, Z \neq 0$, the solution for α (equation 13) is no longer as simple as equation 9. Instead, equation 13 becomes

$$2\pi f_{\mathsf{TX}} \left\{ \frac{1}{c} \Big[\quad X \sin\phi_0 + Y \left(\cos^2\phi_0 - \sin^2\alpha\right)^{\frac{1}{2}} + Z \sin\alpha \Big] - t_{\mathsf{diff}} \right\} = \psi_{\mathsf{OBS}} + n2\pi \qquad (14)$$

which must be solved for α.

Grouping terms, equation 14 can be written as

$$Y \left(\cos^2\phi_0 - \sin^2\alpha\right)^{\frac{1}{2}} + Z\sin\alpha = \left[\frac{\psi_{\mathsf{OBS}} + n2\pi}{2\pi f_{\mathsf{TX}}} + t_{\mathsf{diff}}\right] c - X\sin\phi_0 \equiv E \qquad (15)$$

where the right-hand side of equation 15 has been defined as the constant E in order to simplify subsequent notation.

Rearranging terms in equation 15 and squaring both sides gives

$$\begin{aligned} Y^2\left(\cos^2\phi_0 - \sin^2\alpha\right) &= \left[E - Z\sin\alpha\right]^2 \qquad (16) \\ &= E^2 - 2EZ\sin\alpha + Z^2\sin^2\alpha \end{aligned}$$

and can be written as a quadratic equation in terms of $\sin\alpha$

$$\left(Y^2 + Z^2\right)\sin^2\alpha - 2EZ\sin\alpha + E^2 - Y^2\cos^2\phi_0 = 0 \qquad (17)$$

The solution to equation 17 is

$$\sin\alpha = \frac{EZ + \left[E^2Z^2 - \left(Y^2+Z^2\right)\left(E^2 - Y^2\cos^2\phi_0\right)\right]^{\frac{1}{2}}}{Y^2+Z^2} \qquad (18)$$

where the positive root is chosen for the positive value of α. Equation 18 is the general form of equation 9.

Several example layouts are chosen to illustrate the variety of solutions when additional offsets are nonzero. Figure 3 shows four examples that correspond to the array configurations for the following radars: bks, mcm, lyr and zho. The first three examples have a nonzero value of Z and the latter (zho) has offsets in all three dimensions. For the first two examples (bks and mcm) the observed phase is chosen to be the same as that shown in Figure 2; $\psi_{\mathsf{OBS}} = -0.39\pi$. For the latter two examples (lyr and zho) a value of $\psi_{\mathsf{OBS}} = +0.39\pi$ is used only for purposes of clarity in the Figure. Two examples are chosen for which the interferometer is located behind the main array ($Y < 0$) as evidenced by the positive gradient in ψ_{TOT} shown in Figures 3a and 3c, while the other two examples illustrate the opposite situation.

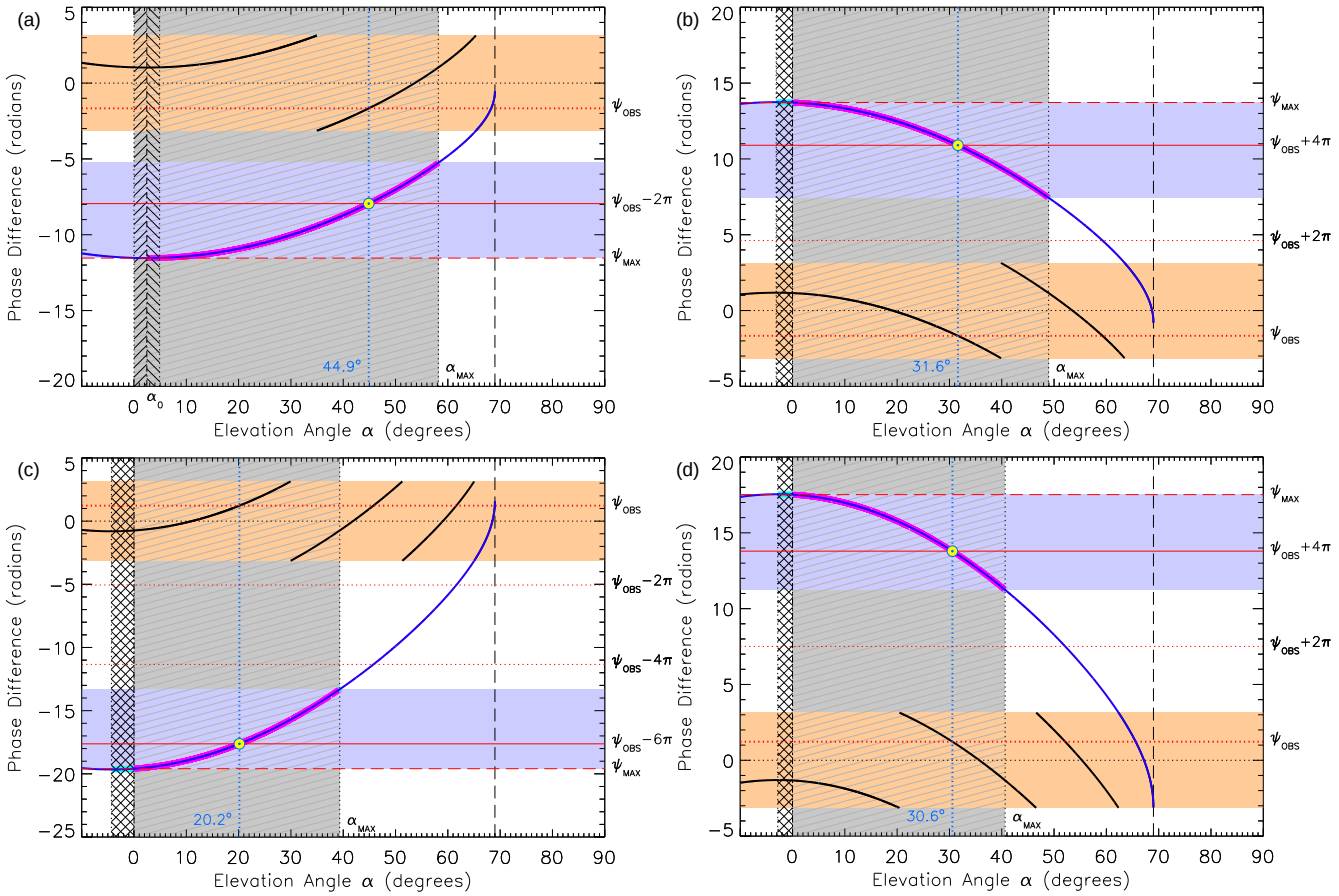

Figure 3. Similar to Figure 2 but for radar layouts where (a) $Y < 0$ and $Z < 0$ for bks, (b) $Y < 0$ and $Z > 0$ for mcm, (c) $Y < 0$ and $Z > 0$ for lyr and (d) $X < 0$, $Y > 0$, $Z < 0$ for zho. For array layouts where (a) $YZ > 0$, a region near $\alpha = 0^\circ$ exists where α cannot be unambiguously determined (marked by a herringbone pattern.) For layouts where (b–d) $YZ < 0$, a region exists where $\alpha < 0^\circ$ is obtained using the basic algorithm (marked by a cross-hatched pattern.) A thick cyan line segment marks the location of negative values of α and where they map to using the algorithm presented here.

One important implication for radars with interferometers that are offset in the $\hat{z}$-direction (nonzero Z) can be seen in Figure 3a. For the bks radar the interferometer is located behind ($Y < 0$) and below ($Z < 0$) the main array. In this case α_0 is positive, i.e., greater than zero. The consequence is that for a small range of $\alpha > \alpha_0$ there is a corresponding value of α below α_0 for which the phase is identical and the range of α values between 0° and $\sim 2\alpha_0$ cannot, therefore, be uniquely determined. (Note the approximate upper limit is due to equation 4; the beam direction depends on α.)

The vertical stripe of herringbone pattern around α_0 in Figure 3a marks this region where the value of α cannot be uniquely determined. Note that the positive solution ($\alpha > \alpha_0$) is obtained but one can-

not rule out that values of $\alpha < \alpha_0$ exist and are aliased into this region. For the bks radar (currently the only radar in the network with this configuration) the range is ∼5°. For any configuration with $YZ > 0$ (the product of the Y and Z offsets), the value of α_0 from equation 11 will be positive and a range of small but indeterminate values of α will exist. The thick magenta line segment in Figure 3a highlights the range of α the algorithm produces: $[\alpha_0, \alpha_{\text{MAX}}]$.

The other important implication for radars with nonzero values of Z is evident in Figures 3b–d. For these radar configurations $YZ < 0$ and the value of α_0 obtained from equation 11 is negative, requiring that plane waves arrive from below the horizon for the values of $\alpha < 0°$. While this situation is perhaps possible when the ground slopes downward in front of the radar (an uncommon situation in most cases), it is more likely that the phase differences mapping to values of $\alpha < 0°$ are in fact aliased from values of $\alpha > \alpha_{\text{MAX}}$. As is the case with choosing the mapping that results in the value of α from the lowest range observable (section 3.1), we assume here that negative values of α are unphysical and set $\alpha_0 = 0°$, thereby mapping these values to near α_{MAX}.

To be clear, the choice of α_0 has the effect of modifying the number of 2π factors used in the mapping from ψ_{OBS} to ψ_{TOT} only for the small range of phase differences that map to the range $[\alpha_0, 0°]$. This range of α, and the corresponding range near α_{MAX}, is highlighted by thick cyan line segments in Figures 3b–d. It can be seen that one consequence of choosing to set $\alpha_0 = 0°$ is to increase the value of α_{MAX}, but only by a small amount compared to the range of $\alpha < 0°$ (e.g., ∼0.2° compared to ∼5° for lyr in Figure 3c.)

Note that while the algorithm currently used to determine α allows for nonzero values of Z, the result is only approximate and differs from the correct value by up to a few degrees. In such cases, the value of α is determined from a modified form of equation 9, where the array separation $d = (Y^2 + Z^2)^{1/2}$ is assumed to be just in the $\hat{y}$-direction, as shown by *Milan et al.* [1997]. This solution is equivalent to assuming $Z = 0$, a separation of $Y = d$ and correcting the final value of α by subtracting the angle the interferometer makes with the x-y plane, i.e., $\tan^{-1}(Z/Y)$. Note that this correction is only an approximation since it does not take into account equation 4 and, more importantly, leads to negative values of α. For the examples shown in Figure 3b–d, the range where $\alpha < 0$ would occur are indicated by the cross-hatched region and α could be as low as approximately -5° using this approximate solution.

4. Algorithm Comparison

In order to demonstrate the impact of using the algorithm derived here, values of α are computed using the current (old) technique, as described by *Milan et al.* [1997] and using equation 18 (new). The algorithms are applied to the measured values of ψ_{OBS} from several radars for a 24-hour period and the resulting values of α are compared.

For radar configurations that only have a nonzero Y component (23 of the 35 operational radars) the differences between the two algorithms are negligible (on the order of 10^{-3} degrees), as would be expected. For most of the other radars the differences are small (less than 1°), with the exception of phases that are close to the boundaries and the values of α are aliased to the upper or lower limits, leading to much larger differences.

Figure 4 shows histograms of the results for two radars; bks and zho. For the Blackstone, Virginia radar (bks) May 31, 2016 was chosen. On this day the radar operated between 10–11 MHz for the entire day. Backscatter was observed at a variety of ranges and from a variety of sources throughout the day, including ground scatter, low-velocity sub-auroral irregularities [*Ribeiro et al.*, 2012], near-range meteor echoes and possibly some F-region backscatter. Correct classification of backscatter can be a difficult task and is not critical to the results shown here [e.g., *Milan et al.*, 2001; *Burrell et al.*, 2015]. The important point is that a distribution of ψ_{OBS} was measured.

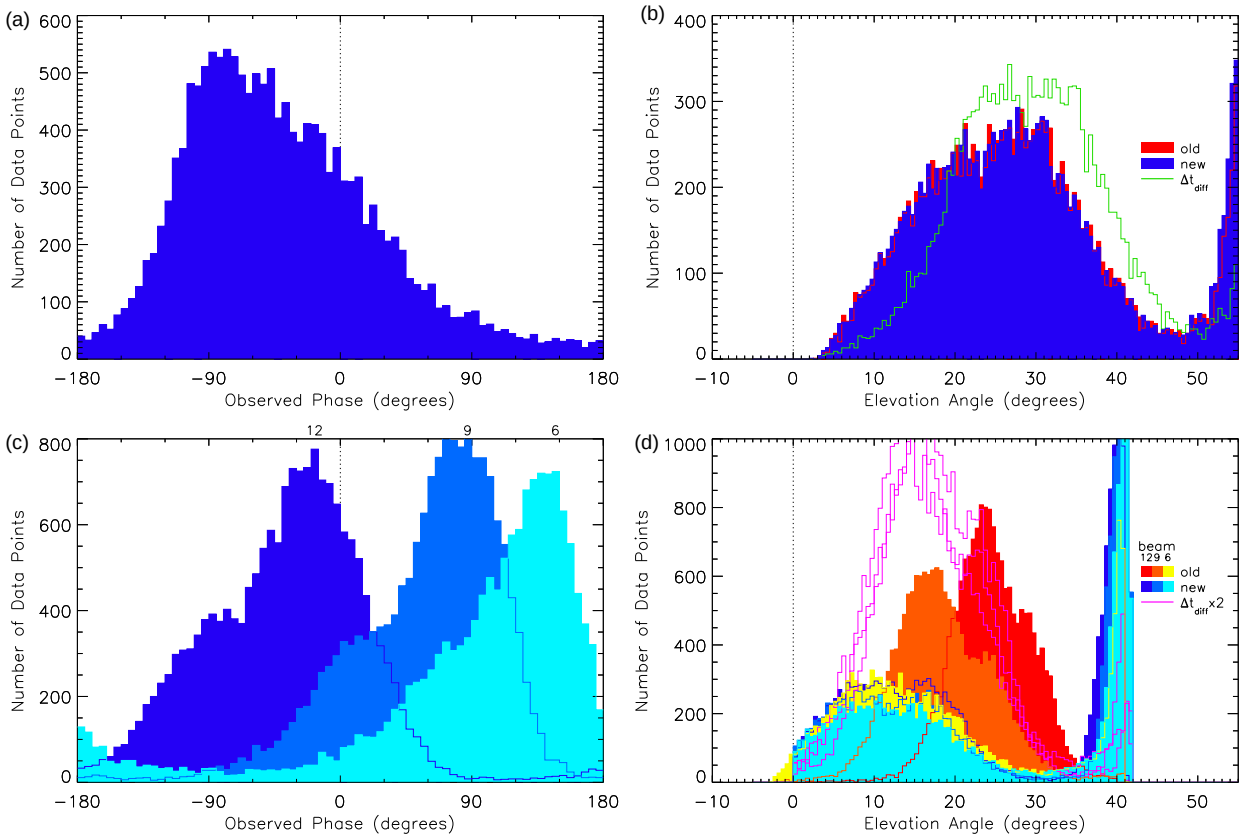

Figure 4. Histograms of the (a) observed phase differences (ψ_{OBS}) on May 31, 2016 from Blackstone, VA and (b) corresponding elevation angles (α) determined using the basic algorithm (red) and equation 18 (blue). Histograms of (c) ψ_{OBS} for three beam directions (6, 9, 12) on April 20, 2016 from Zhongshan Station radar (zho) and (d) the corresponding values of α determined using the basic algorithm (red, orange, yellow) and equation 18 (blue shades). Green and magenta histograms in (b) and (d) represent values of α obtained using an alternative value of t_{diff} in equation 18.

Figure 4a shows the distribution of ψ_{OBS} for beam 18 of the Blackstone, Virginia radar (bks) directed ~21° off of the boresight direction. The distribution is seen to peak near -90° but it is clear that some aliasing must be occurring since there are counts for every phase in the range [-π,π].

Figure 4b shows distributions of α computed using the old (red) and new (blue) algorithms. The distributions are similar and only small differences are present, ranging from ~0.5–1.5° and unlikely to have much affect on subsequent analyses, such as geolocation.

One aspect worth noting about the distributions shown in Figure 4b is the region near $\alpha = 0°$ where there are no counts. This is the region discussed in section 3 for radar layouts with $YZ > 0$ where a small range of α near 0° cannot be unambiguously determined. In this case values of $\alpha < \alpha_0$ are assigned to their corresponding values where $\alpha > \alpha_0$. Note also that α_{MAX} for this beam is ~55°. Values of

α greater than this limit are aliased into the range of lower values.

Another aspect of Figure 4b worth noting is the narrow peak near α_{MAX}, which seen in both distributions. Although not essential to the focus of this work it is curious that a peak would occur near the upper limit of α. One possible explanation is that backscatter from the radar back lobe is the source of these returns [*Milan et al.*, 1997; *André et al.*, 1998]. However, an alternate explanation is that the value of t_{diff} used to compute α is not correct.

Using a technique similar to that described by *Ponomarenko et al.* [2015] (where the behavior of ψ_{OBS} for ground scatter returns at far ranges is used to determine t_{diff}), a value of $t_{\mathsf{diff}} = -0.330\mu$s is identified and used to recompute α. The distribution using this value of t_{diff} is shown in Figure 4b as a green histogram. Note that the peak near α_{MAX} has been significantly reduced and the broader peak near 25° has shifted to ∼30°. While a more careful analysis is needed, the results here suggest that the likely source of the narrow peak near α_{MAX} is due to the incorrect value of t_{diff}, shifting the actual phases beyond the value that maps to α_0 so that they are subsequently aliased towards α_{MAX}. Note that only a small change (relative to its magnitude) in the value of t_{diff} (8 ns) can have a significant effect on the observed values of α. The differences seen here range from ∼5–15°, much larger than any difference that can be attributed to using the old algorithm.

The second example shown in Figure 4 comes from the radar located at the Zhongshan Station in Antarctica (zho). The day chosen for this radar is April 20, 2016 and backscatter was observed from a variety of sources but primarily that of ionospheric origin, including both direct and multi-hop E- or F-region backscatter. The measured values of ψ_{OBS} are shown in Figure 4c for three different beams (12, 9 and 6), corresponding to azimuthal beam directions of $\phi_0 = -5°, 5°, 15°$.

The peak of the phase distribution is seen to vary significantly with beam direction, as might be expected when observing backscatter from an extended source region from different directions. Because the altitude of this region is expected to be relatively constant it is not, however, expected that the peak in the distribution of α would also vary with beam direction, as can be seen to occur in the distributions shown in Figure 4d (red, orange and yellow). Note that the old algorithm is used here despite the fact that it is not intended to be used for radar layouts with nonzero X values. With no alternative it can be seen that use of the old algorithm gives results that are not consistent with expectations.

Figure 4d shows that using the new algorithm results in a more uniform distribution of α across beams. Although some variation is seen in the peaks of these distributions (blue shades), it is small and they are more consistent with the expectation that the distribution of α does not vary significantly with beam direction. Note that the narrow peak near α_{MAX} is also evident in these histograms (blue shades.) As shown for the previous case, a small change in t_{diff} to -0.195 ns significantly reduces these peaks, as shown by the magenta lines in Figure 4d. While there is no significant ground scatter present to use in order to justify this value of t_{diff} [e.g., *Ponomarenko et al.*, 2015] and specific details of the histograms (other than their peaks) are relatively unimportant for this work, it is important to note that reasonable results are achievable for a radar with a significant offset in the $\hat{x}$-direction.

Finally, it is noted that values of $\alpha < 0°$, deemed unphysical for this study, are seen in the distributions resulting from use of the old algorithm (red, orange and yellow histograms in Figure 4d.) These values (most notable in beam 6, yellow histogram) are also present in other radar configuration for which $YZ < 0$ and result from the incorrect treatment of a nonzero Z value. They are no longer present when using the algorithm presented here (blue shaded and magenta histograms.)

5. Discussion

The results shown here suggest that the algorithm presented is correct for determining the value of α of signals measured by SuperDARN radars with a variety of interferometer layouts. Ideally, it would be tested in such a way as to validate the correctness of the algorithm, however, such a test would require measurements of a scattering source at a known location. While such a source does not exist in the field-of-view (FOV) of the Zhongshan radar (zho), a high-power, radio frequency facility (ionospheric heater) operated by the European Incoherent Scatter (EISCAT) Scientific Association at Tromsö, Norway is located in the FOVs of two SuperDARN radars. Two studies by *Yeoman et al.* [2001, 2008] used ionospheric irregularities produced by the EISCAT heater (and assumptions about real and virtual

propagation paths [*Chisham et al.*, 2008]) as a calibration source for interferometer measurements of the SuperDARN radars located in Hankasalmi, Finland (han) and Pykkvibaer, Iceland (pyk).

Unfortunately the configurations of these radars are such that differences between the old and new algorithms would only be on the order of 1° or less and any assessment of the correctness of the new algorithm would be inconclusive. However, a new radar facility planned for installation in Ireland in the coming years will have a FOV that also contains the EISCAT heater. For this radar an interferometer array with additional antenna elements is planned. The special interferometer array will allow for observations of irregularities produced by the EISCAT heater with varying values of the X offset. It is hoped that these types of experiments will help in validating the algorithm presented here.

For completeness, there is a special algorithm that was developed for the Goose Bay, Labrador radar (gbr) which originally had a very large offset in the $\hat{x}$-direction; $X = -15.5$m. The algorithm, described by *Baker and Greenwald* [1988] and *André et al.* [1998], calls for the solution to the intersection of two phase cones; one determined by ϕ, given here by equation 4, and the other by the phase difference between the main and interferometer arrays. (Note that in these studies the coordinate system is different than the one used here.)

The algorithm was implemented using an iterative approach to find the solution, however it only works for radars with interferometers that are located in front of the main array, i.e., $Y > 0$. In addition, it was not intended to be used when Z is also nonzero and never adapted for the general case. The solution given by equation 18 is intended to be general and can be applied to any of the radars listed in Table 1 and to any future radars.

6. Summary

SuperDARN radars are equipped with interferometer arrays for the purpose of determining α – the elevation angle of backscattered signals. Most radars are configured with interferometer arrays that are offset only in the direction of the boresight and the task is relatively straightforward. In these cases a comparatively simple algorithm (described by *Milan et al.* [1997] and given in equation 9) is used to determine α with satisfactory results.

This algorithm can also be used in the somewhat less common situation where the interferometer has an additional offset in the vertical direction, but the results are approximate and small errors of up to ∼1° can occur. In addition, the algorithm can produce values of α that are negative; an unlikely scenario for most radar configurations. For radars with interferometers offset in all three dimensions the algorithm is not applicable.

A generalized algorithm is presented here that can be used for determining α for SuperDARN radars with interferometers offset in any or all three dimensions. The algorithm is applied to observations obtained from SuperDARN radars with a variety of interferometer configurations and results are compared with those obtained from the simpler algorithm. For situations where the interferometer is offset only along the boresight direction the results differ by an inconsequential amount. In the case where an additional offset in the vertical direction is present the generalized algorithm correctly accounts for the dependence of the beam direction on α and small differences of up to ∼1° are observed. For the case where the interferometer is offset in all three dimensions it is demonstrated that the generalized algorithm produces results that are consistent with expectations, i.e., no significant dependence of α on radar beam direction is observed.

Two subtleties of particular interferometer configurations are discussed. The first is a small range near $\alpha = 0°$ where α cannot be unambiguously determined and the algorithm produces values above the minimum observable angle (α_0). The second is the treatment of negative values of α that are produced by the simpler algorithm as a consequence of the interferometer configuration. In the generalized algorithm negative values of α are deemed unphysical and are no longer obtained.

While a few issues remain in making reliable and unambiguous determinations of elevation angles from SuperDARN radars; such as a robust method for calibrating the phase difference associated with the electrical signal paths in radars (t_{diff}) [*Ponomarenko et al.*, 2015; *Burrell et al.*, 2016], the aliasing associated with measuring the relative phase difference with a single interferometer [*McDonald et al.*, 2013] and discrimination between front and back lobe backscatter [*Milan et al.*, 1997; *Burrell et al.*, 2015]; the algorithm described here represents a clear

improvement in the capability of SuperDARN to make interferometer measurements and significantly reduces any constraints placed on future interferometer configurations. The improved capability of determining α will undoubtedly enhance many aspects of SuperDARN observations such as a more accurate geolocation of backscatter and the estimation of ionospheric quantities.

Acknowledgments. This work was made possible by continued support of the NSF; grants AGS–0838356, AGS–1341925 and AGS–1655193. The author acknowledges the use of SuperDARN data. SuperDARN is a collection of low-power scientific HF radars funded by the national scientific funding agencies of Australia, Canada, China, France, Italy, Japan, Norway, South Africa, United Kingdom and United States of America. Data and analysis software are available from `http://superdarn.thayer.dartmouth.edu` or other SuperDARN institutions.

References

André, D., G. J. Sofko, K. Baker, and J. MacDougall (1998), SuperDARN interferometry: Meteor echoes and electron densities from groundscatter, *J. Geophys. Res.*, *103*(A4), 7003–7015.

André, R., C. Hanuise, J.-P. Villain, and J.-C. Cerisier (1997), HF radars: Multifrequency study of refraction effects and localization of scattering, *Radio Sci.*, *32*(1), 153–168.

Baker, K. B., and R. A. Greenwald (1988), The vertical angle of arrival of high-frequency signals propagating from Thule to Goose Bay, *Johns Hopkins APL Technical Digest*, *9*(2), 121–130.

Baker, K. B., R. A. Greenwald, and R. T. Tsunoda (1983), Very high latitude F-region irregularities observed by H.F. radar backscatter, *Geophys. Res. Lett.*, *10*, 904.

Bland, E. C., A. J. McDonald, S. de Larquier, and J. C. Devlin (2014), Determination of ionospheric parameters in real time using SuperDARN HF radars, *J. Geophys. Res.*, *119*, 5830–5846, doi: 10.1002/2014JA020076.

Burrell, A. G., S. E. Milan, G. W. P. T. K. Yeoman, and M. Lester (2015), Automatically determining the origin direction and propagation mode of high-frequency radar backscatter, *Radio Sci.*, *50*, 1225–1245, doi: 10.1002/2015RS005808.

Burrell, A. G., T. K. Yeoman, S. E. Milan, and M. Lester (2016), Phase calibration of interferometer arrays at high-frequency radars, *Radio Sci.*, *51*(9), 1445–1456, doi:10.1002/2016RS006089.

Chisham, G., M. Lester, S. E. Milan, M. P. Freeman, W. A. Bristow, A. Grocott, K. A. McWilliams, J. M. Ruohoniemi, T. K. Yeoman, P. L. Dyson, R. A. Greenwald, T. Kikuchi, M. Pinnock, J. P. S. Rash, N. Sato, G. J. Sofko, J.-P. Villain, and A. D. M. Walker (2007), A decade of the Super Dual Auroral Radar Network (SuperDARN): Scientific achievements, new techniques and future directions, *Surv. Geophys.*, *28*, 33–109.

Chisham, G., T. K. Yeoman, and G. J. Sofko (2008), Mapping ionospheric backscatter measured by the SuperDARN HF radars: Part 1: A new empirical virtual height model, *Ann. Geophysicae*, *26*, 823–841.

Custovic, E., A. J. McDonald, J. Whittington, D. Elton, T. A. Kane, and J. C. Devlin (2013), New antenna layout for a SuperDARN HF radar, *Radio Sci.*, *48*, 722–728, doi:10.1002/2013RS005156.

de Larquier, S., P. Ponomarenko, A. J. Ribeiro, J. M. Ruohoniemi, J. B. H. Baker, K. T. Sterne, and M. Lester (2013), On the spatial distribution of decameter-scale subauroral ionospheric irregularities observed by SuperDARN radars, *J. Geophys. Res.*, *118*, 5244–5254, doi:10.1002/jgra.50475.

Gillies, R. G., G. C. Hussey, G. J. Sofko, K. A. McWilliams, R. A. D. Fiori, P. Ponomarenko, and J.-P. St.-Maurice (2009), Improvement of SuperDARN velocity measurements by estimating the index of refraction in the scattering region using interferometry, *J. Geophys. Res.*, *114*, A07305, doi: 10.1029/2008JA013967.

Greenwald, R. A., K. B. Baker, R. A. Hutchins, and C. Hanuise (1985), An HF phased-array radar for studying small-scale structure in the high-latitude ionosphere, *Radio Sci.*, *20*, 63.

Greenwald, R. A., K. B. Baker, J. R. Dudeney, M. Pinnock, T. B. Jones, and et. al. (1995), DARN/SuperDARN: A global view of the dynamics of high-latitude convection, *Space Sci. Rev.*, *71*, 761.

Hughes, J. M., W. A. Bristow, R. A. Greenwald, and R. J. Barnes (2002), Determining characteristics of HF communications links using SuperDARN, *Ann. Geophysicae*, *20*, 1023–1030.

McDonald, A. J., J. Whittington, S. de Larquier, E. Custovic, T. A. Kane, and J. C. Devlin (2013), Elevation angle-of-arrival determination for a standard and a modified SuperDARN HF radar layout, *Radio Sci.*, *48*, 709–721, doi:10.1002/2013RS005157.

Milan, S. E., T. B. Jones, T. R. Robinson, E. C. Thomas, and T. K. Yeoman (1997), Interferometric evidence for the observation of ground backscatter originating behind the CUTLASS coherent HF radars, *Ann. Geophysicae*, *15*, 29–39.

Milan, S. E., M. Lester, J. R. Dudeney, R. A. Greenwald, G. Sofko, J. P. Villain, and R. P. Lepping (2001), The excitation of convection in the cusp region as observed by the SuperDARN radars, *Adv. Space Res.*, *27*, 1373.

Ponomarenko, P., N. Nishitani, A. V. Oinats, T. Tsuya, and J.-P. St.-Maurice (2015), Application of ground scatter returns for calibration of HF interferometry data, *Earth Planets Space*, *67*(138), doi: 10.1186/s40623-015-0310-3.

Ponomarenko, P. V., A. V. Koustov, J.-P. St-Maurice, and J. Wiid (2011), Monitoring the F-region peak electron density using HF backscatter interferometry, *Geophys. Res. Lett.*, *38*, L21102, doi: 10.1029/2011GL049675.

Ribeiro, A. J., J. M. Ruohoniemi, J. B. H. Baker, L. B. N. Clausen, R. A. Greenwald, and M. Lester (2012), A survey of plasma irregularities as seen by the midlatitude Blackstone SuperDARN radar, *J. Geophys. Res.*, *117*, A02311, doi:10.1029/2011JA017207.

Villain, J. P., R. A. Greenwald, and J. F. Vickrey (1984), HF ray tracing at high latitudes using measured meridional electron density distributions, *Radio Sci.*, *19*, 359.

Yeoman, T. K., D. M. Wright, A. J. Stocker, and T. B. Jones (2001), An evaluation of range accuracy in the Super Dual Auroral Radar Network over-the-horizon HF radar systems, *Radio Sci.*, *36*(4), 801–813, doi: 10.1029/2000RS002558.

Yeoman, T. K., G. Chisham, L. J. Baddeley, R. S. Dhillon, T. J. T. Karhunen, T. R. Robinson, A. Senior, and D. M. Wright (2008), Mapping ionospheric backscatter measured by the SuperDARN HF radars – part 2: Assessing SuperDARN virtual height models, *Ann. Geophysicae*, *26*, 843–852, doi:10.5194/angeo-26-843-2008.

Corresponding author: S. G. Shepherd, Thayer School of Engineering, Dartmouth College, 14 Engineering Dr., Hanover, NH 03755, USA. (simon.g.shepherd@dartmouth.edu)

(Received _____.)